

Article

The Surface Modification of ZrO₂ Film by Zr/Nb Ion Implantation and First-Principles Calculation

Yuan Gao , Luyao Wang and Dejun Li * 

College of Physics and Materials Science, Tianjin Normal University, Tianjin 300387, China; yuangao.cn@outlook.com (Y.G.); wangluyao_97@163.com (L.W.)

* Correspondence: dejunli@tjnu.edu.cn

Abstract: Zirconium dioxide (ZrO₂) possesses numerous advantages such as high mechanical strength, a low friction coefficient, excellent optical properties, and an extended lifespan. Consequently, ZrO₂ has a broad research foundation and practical significance in functional films and wear-resistant coatings. However, it suffers from brittleness and low ductility when used as a bio-coating material. In this study, a ZrO₂ film was fabricated on Si (100) and titanium alloy substrates using a magnetron sputtering system. Subsequently, Zr and Nb ions were implanted into the film at varying doses, but with consistent energy levels. The analysis focused on the film's microstructure, mechanical properties, hydrophilicity, and corrosion resistance. The results demonstrate a significant improvement in the hydrophilicity and corrosion resistance of the ZrO₂ film following the implantation of Zr and Nb ions. First-principles calculations based on density functional theory (DFT) principles indicated that, with increasing doping concentrations of Zr and Nb in the ZrO₂ model, the stability of the model increased gradually, thereby enhancing its corrosion resistance. The developed product has propelled rapid advancements in fields such as biomedical implants.

Keywords: ZrO₂ film; ion implantation; first-principles calculations; structural stability



Citation: Gao, Y.; Wang, L.; Li, D. The Surface Modification of ZrO₂ Film by Zr/Nb Ion Implantation and First-Principles Calculation. *Coatings* **2023**, *13*, 1696. <https://doi.org/10.3390/coatings13101696>

Academic Editors: Egemen Avcu, Yasemin Yildiran Avcu and Mert Guney

Received: 10 September 2023
Revised: 21 September 2023
Accepted: 26 September 2023
Published: 27 September 2023



Copyright: © 2023 by the authors. Licensee MDPI, Basel, Switzerland. This article is an open access article distributed under the terms and conditions of the Creative Commons Attribution (CC BY) license (<https://creativecommons.org/licenses/by/4.0/>).

1. Introduction

Zirconium dioxide (ZrO₂) films are widely employed in biomedical coatings due to their excellent corrosion resistance and mechanical properties [1]. To extend the lifespan of implant materials, there is a heightened demand for enhanced corrosion resistance of these ZrO₂ coatings [2–7]. Chauhan, V. et al. have demonstrated that nearly any material subjected to ionizing radiation, such as gamma rays or X-rays, can induce changes in the material's microstructural characteristics [8]. Heavy ion irradiation, in particular, can alter the grain morphology of ZrO₂ [9,10]. Current research on ZrO₂ primarily focuses on the influence of deposition parameters on the film's structure, morphology, and some characteristics. However, there is relatively limited research on the doping of metal particles into ZrO₂ films, which can significantly impact their structure and relevant properties [11–14]. To overcome the inherent shortcomings of ZrO₂, researchers have conducted surface modification studies. The primary approach involves depositing modifying elements that meet the desired requirements to enhance the film's performance. Abd El-Aal, M. et al. demonstrated that Au-Pd alloy films prepared by DC magnetron sputtering exhibited superior catalytic activity compared to Au films [15]. Therefore, this study explores the doping of other metal ions into the ZrO₂ lattice to produce ZrO₂ films with superior corrosion resistance and thermal stability. Zirconium (Zr) and niobium (Nb) inherently possess good corrosion resistance [16,17], and their injection onto the surface enhances their corrosion resistance by allowing them to exhibit their typical chemical properties [18–20]. In recent years, researchers have discovered that niobium materials show significant potential in the field of photocatalysis, such as their inhibitory effects on U87-MG cancer cells and suppression of gaseous toxic byproducts [21,22]. Furthermore, Nb ion implantation forms

compounds on the surface, which may contribute to improved corrosion resistance. These coatings hold promise as corrosion-resistant materials [23–25]. For instance, Zr and oxygen ion implantation on magnesium alloys results in ZrO_2 -containing films, reducing the corrosion rate of the treated substrates, as indicated by electrochemical and weight loss tests [26].

Studying the structural aspects of point defects in crystals can provide a better understanding of a material's macroscopic and microscopic properties. In comparison to experimental investigations, theoretical calculations offer a more direct approach to studying these defects, providing insights into a sample's intrinsic plastic properties and structural stability. Therefore, researching the microstructure of Zr/Nb- ZrO_2 is of paramount importance. To elucidate the microstructure of Zr/Nb- ZrO_2 , calculations of its formation energy and binding energy were performed. Additionally, the fundamental physical and electronic properties of Zr/Nb- ZrO_2 , including the total density of states and partial density of states, were computed.

In this study, we prepared ZrO_2 films with varying Zr and Nb ion implantation doses on biocompatible titanium alloy and silicon substrates using magnetron sputtering and plasma immersion ion implantation systems. We investigated the interrelationships between composition and microstructural properties and discussed the impact of implantation doses of Zr/Nb ions on the film's phase structure, contact angle, mechanical properties, and corrosion resistance. Dual-ion implantation demonstrates the synergistic effect of Zr/Nb, providing a more comprehensive exploration of how different injection ratios affect the performance of ZrO_2 films. Furthermore, first-principles calculations were introduced to further support the mechanisms behind the influence of dual-ion implantation on structural stability and corrosion resistance properties.

2. Materials and Methods

2.1. Preparation of Zr/Nb- ZrO_2 Films

On silicon (100) and titanium alloy (Ti-6Al-4V) substrates, ZrO_2 films were deposited using a magnetron sputtering system (FJL560CI2, Shenyang Scientific Instrument Co., Ltd., Chinese Academy of Sciences, Shengyang, China). Subsequently, Zr and Nb ions were implanted into the near-surface region of the ZrO_2 films using a plasma immersion ion implantation and deposition system (PIII and D-700, Tongchuang, China), as shown in Figure 1.

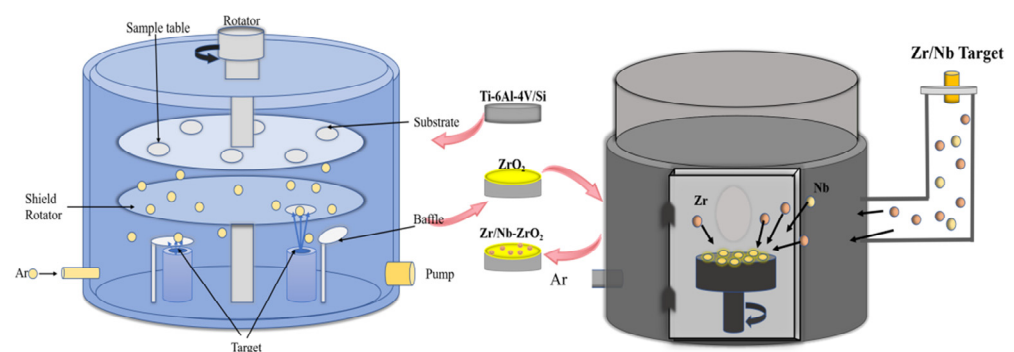


Figure 1. Schematic diagram of the magnetron sputtering system (FJL560CI2) and plasma immersion ion injection system (PIII and D-700).

For samples based on silicon substrates, they were employed to evaluate the crystal's microstructure and mechanical properties. Samples based on titanium alloy substrates were used to assess corrosion resistance and hydrophilicity. The ZrO_2 target (4 mm thickness, 99.99% purity, Beijing ZhongCheng Advanced Material Technology Co., Ltd., Beijing, China) material was controlled by radio frequency (RF) cathode power supplies. The target–substrate distance was established at 50 mm. The system was evacuated until the pressure was less than 4.5×10^{-4} Pa. Then, at a pressure of 5 Pa, high-purity (99.99%)

argon gas was introduced into the vacuum chamber. Under conditions of a constant bias voltage of 40 V, an RF power of 80 W, and an operating pressure of 0.5 Pa, the sample holder was rotated sequentially onto the ZrO₂ target to control the film's thickness by varying the sputtering time. The resulting film's thickness was approximately 400 nm.

In the plasma immersion ion implantation and deposition system (PIII and D-700, China), a mixed target of Zr (97.5%) and Nb (2.5%) was employed as the source for zirconium and niobium ions. When the vacuum chamber pressure reached 7.5×10^{-4} Pa, high-purity argon gas (99.999% purity) was introduced to achieve a working pressure of 5×10^{-3} Pa. The experimental parameters are shown in Table 1.

Table 1. The experiment parameters of Zr/Nb-ZrO₂ film by PIII.

Experiment Groups	Zr/Nb-ZrO ₂ 1	Zr/Nb-ZrO ₂ 2	Zr/Nb-ZrO ₂ 3
Voltage (kV)	−10	−10	−10
Magnetic bias (V·s)	10;10	10;10	10;10
Pulse frequency (Hz)	6	6	6
Time (min)	50	60	70

2.2. Surface Morphology and Structural Composition

The surface morphology of the samples was observed using scanning electron microscopy (SEM, SU-8010, Hitachi, Tokyo, Japan). The samples were analyzed using an X-ray diffractometer (XRD, D8 Advance, Bruker, Mannheim, Germany) to determine the phase composition and crystal orientation. Scanning was performed using Cu-K α radiation with a wavelength of 1.54Å, in the range of 20–80°, with step and dwell times of 0.02 s and 7.76 s, respectively. Subsequently, the obtained data were analyzed using Jade 6.5 software. Atomic force microscopy (AFM, Multimode 8, Bruker, Germany) was employed to measure the surface roughness of the tested samples. The measurements were then analyzed using NanoScope Analysis 1.5 software. The composition of the samples was determined using X-ray photoelectron spectroscopy (XPS, PHI5000, Versaprobe, Chigasaki, Japan) with an Al-K α source. The obtained raw data were subjected to peak fitting analysis using XPS peak 41 software.

2.3. Mechanical Properties

The hardnesses and elastic moduli of the films were analyzed using an XP nanoindenter (STEP 6, Anton Paar, Graz, Austria), with the maximum indentation depth maintained at 15% of the coating thickness. Each sample underwent three repeated experiments.

2.4. Water Contact Angle Assay

The water contact angles of all samples were measured using a static contact angle measurement instrument (CAMKSV021733, NUNC). A 1 μ L deionized water droplet was placed on different areas of the sample's surface. The average of these 10 measurements was taken as the experimental result (two decimal places were retained), and the contact angle values and water droplet images were obtained.

2.5. Corrosion Resistance

The corrosion resistance levels of all samples were measured in a phosphate-buffered saline solution (PBS, pH 7.4, HyClone, Seattle, WA, USA) environment using an electrochemical workstation (CHI604E A17961, Shanghai Chenhua Instrument Co., Ltd., Shanghai, China). The samples served as the working electrodes, platinum was used as the counter electrode, and a saturated calomel electrode was employed as the reference electrode. The test voltage ranged from −1.0 to 0.5 V, with a scanning rate of 0.01 mV/s.

2.6. First Principle Calculation

The CASTEP module within the density functional theory (DFT) framework was employed for theoretical calculations, and the stability and mechanical properties of the ZrO_2 system, as well as the ZrO_2 system doped with Zr/Nb, were estimated. To ensure the accuracy of the simulations in this study, ultra-soft pseudopotentials and the generalized gradient approximation with Perdew–Burke–Ernzerhof (GGA-PBE) exchange–correlation potential were utilized. For the calculations, a cutoff energy of 300 eV was set for the plane-wave expansion of the ZrO_2 system and the ZrO_2 system doped with Zr/Nb. The most accurate convergence precision was chosen as per the default method for this part of the calculation. The k-point mesh which was used was either $11 \times 11 \times 15$ or $15 \times 15 \times 10$, depending on whether it was for the undoped system or the Zr/Nb-doped system in the Brillouin zone integration. These parameters were carefully chosen to ensure precise calculations, and both the cutoff energy and k-point mesh contributed to the excellent convergence of this study [27–29]. These data correspond to the physical experimental results, as they were calculated based on the same observed trends. They are not expected to be identical, but rather, representative of the experimental data.

3. Results and Discussion

3.1. Microstructure and Mechanical Properties

Figure 2 shows the SEM images of four groups of samples (ZrO_2 , Zr/Nb- ZrO_2 1 (50 min); Zr/Nb- ZrO_2 2 (60 min); and Zr/Nb- ZrO_2 3 (70 min)). Under the sputtering conditions used in this study, the surfaces of the ZrO_2 films appeared to be dense and smooth, as shown in Figure 2a. The cross-sectional images of the sputtered films are depicted in Figure 2e. However, following the injection of Zr and Nb ions, some small clusters formed on the surface due to atomic collisions [30]. This resulted in slightly larger particles on the surface of the post-injection samples, as illustrated in Figure 2b–d.

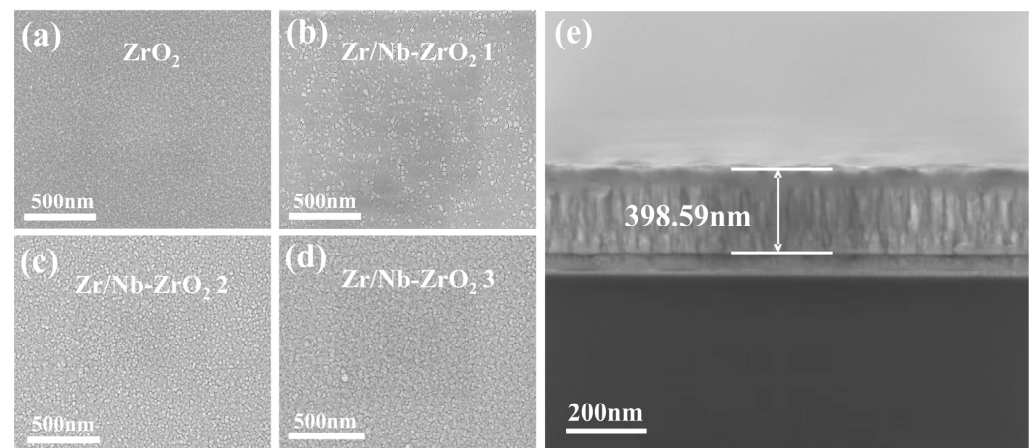


Figure 2. SEM image of the surface topography under magnetron sputtering and different injection conditions (a–d), and the cross-sectional SEM image (e).

Figure 3 presents the XRD pattern of the four sample groups, revealing the crystal structures of ZrO_2 films under various injection conditions. It is evident that these films exhibit well-defined crystal orientations, with the (202) crystallographic direction being the strongest, indicating t- ZrO_2 . After the injection of zirconium and niobium ions, two new Nb_2O_5 peaks of varying intensities emerged. Notably, when the injection time reached 70 min, the $(-2,1,5)$ and $(-2,1,6)$ peaks of Nb_2O_5 became the most pronounced. This signifies that with the increasing injection time (and hence dosage), the prepared Zr/Nb- ZrO_2 introduced new Nb_2O_5 crystal orientations. This observation confirms that Nb ions combine with oxygen to form Nb_2O_5 , and as the dosage increases, the crystal orientation gradually strengthens. Nb and Nb_2O_5 possess desirable traits such as good ductility

and corrosion resistance [31], further ameliorating the inherent brittleness and processing challenges of pure ZrO_2 [32].

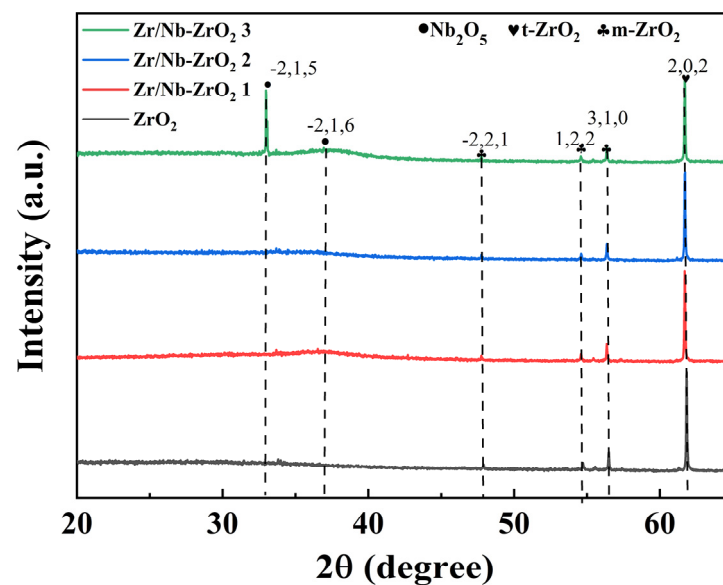


Figure 3. XRD pattern of Zr/Nb-ZrO₂.

Figure 4a–d shows the AFM three-dimensional images of the four sample surfaces, while Figure 4e displays the arithmetic average roughness (Ra), and Figure 4f presents the root-mean-square roughness (Rq) of the four samples' surfaces. The results indicate that the surface of the ZrO_2 film is dense, smooth, and characterized by small grains. However, after the injection of Zr and Nb ions, there is an increase in grain size and particle dimensions, leading to an elevation in surface roughness. Notably, the Zr/Nb-ZrO₂ 2 sample exhibits the highest roughness. This increase in roughness can be attributed to the injection of particles, which results in a slight expansion of atomic dimensions and the enlargement of grains, consequently leading to a noticeable rise in surface roughness [24,33]. Additionally, ion bombardment on the surface creates defects and voids, which are favorable for the growth of new films. Within a certain concentration range, the injection of Zr and Nb (primarily Zr) can lead to solid solution strengthening and high dislocation density, blocking the movement of defects and resulting in increased hardness and reduced ductility, which aligns with the hardness results from nanoindentation testing [34].

XPS analysis was employed to further investigate the chemical composition of the samples. As shown in Figure 5a, after the implantation of Zr and Nb ions, the samples exhibited prominent Zr peaks, while the enhancement of Nb peaks was less pronounced, primarily due to the relatively low initial Nb content in the target material. The surface Nb content of the samples is provided in Table 2, indicating an increasing Nb content. Since the target was a mixture of Zr and Nb, the increment in Nb content was not strictly proportional. High-resolution narrow spectra for $\text{Zr}3d$, $\text{Nb}3d$, and $\text{O}1s$ are presented in Figure 5b–d. The $\text{Zr}3d$ spectrum displayed peaks at 182.73 eV and 185.40 eV, corresponding to ZrO_2 [35]. In the $\text{Nb}3d$ spectrum, peaks at 208.11 eV (Nb_2O_5) and 210.90 eV (Nb_2O_5) indicated that Nb in the post-injection samples primarily existed in the form of Nb_2O_5 [36,37], as Nb readily combines with oxygen to form oxides [38]. Simultaneously, the $\text{O}1s$ spectrum revealed peaks at 530.5 eV (ZrO_2) and 530.9 eV (Nb_2O_5), while the peak at 531.4 eV represented adsorbed oxygen from the ambient air [39,40]. Consequently, the introduction of Zr and Nb ions into ZrO_2 did not alter its original chemical composition, but led to the formation of a new compound, Nb_2O_5 .

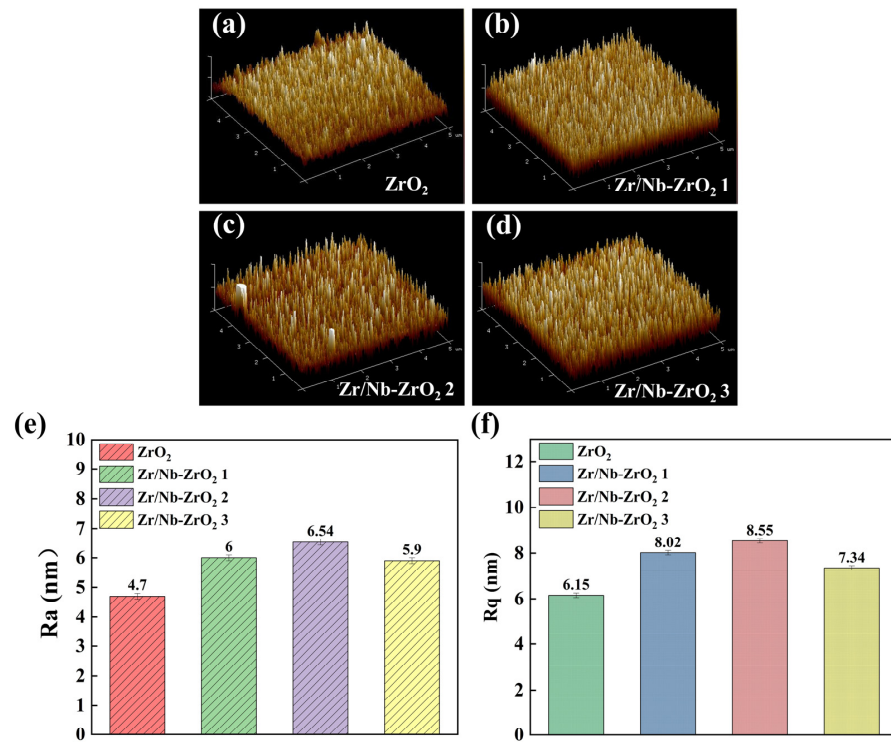


Figure 4. 3D images of different surface morphologies and roughnesses by AFM, (a) ZrO₂, (b) Zr/Nb-ZrO₂ 1, (c) Zr/Nb-ZrO₂ 2, and (d) Zr/Nb-ZrO₂ 3. (e) The Ra roughness; (f) the Rq roughness.

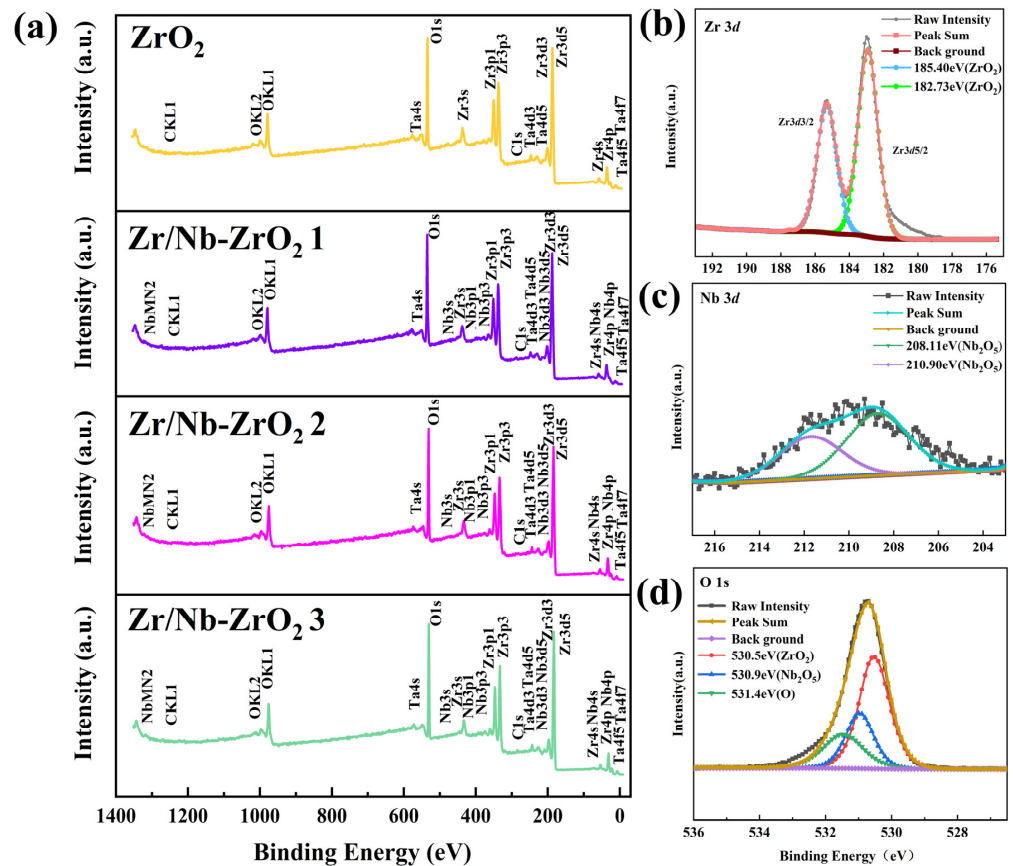


Figure 5. (a) XPS spectra of four groups of samples. (b) Zr3d, (c) Nb3d, and (d) O1s XPS spectra of Zr/Nb-ZrO₂.

Table 2. Atomic percent of the Zr/Nb-ZrO₂ film.

Sample	Zr/Nb-ZrO ₂ 1	Zr/Nb-ZrO ₂ 2	Zr/Nb-ZrO ₂ 3
Relative percent of Nb (%)	0.8	0.59	1.02

Figure 6a–d depict the hardness load-unload curves of the samples. It can be observed from the graphs that the maximum loads were roughly similar, with no significant difference in the unloading displacements. As shown in Figure 6e,f, Zr/Nb-ZrO₂ 3 exhibited the highest hardness, measuring 13.569 GPa, while Zr/Nb-ZrO₂ 1 demonstrated the highest elastic modulus at 240.08 GPa. This enhancement in mechanical properties may be attributed to the formation of a Nb₂O₅ thin film with good plasticity due to ion bombardment [41]. Consequently, these findings suggest that the ZrO₂ films exhibit improved deformation resistance after ion implantation.

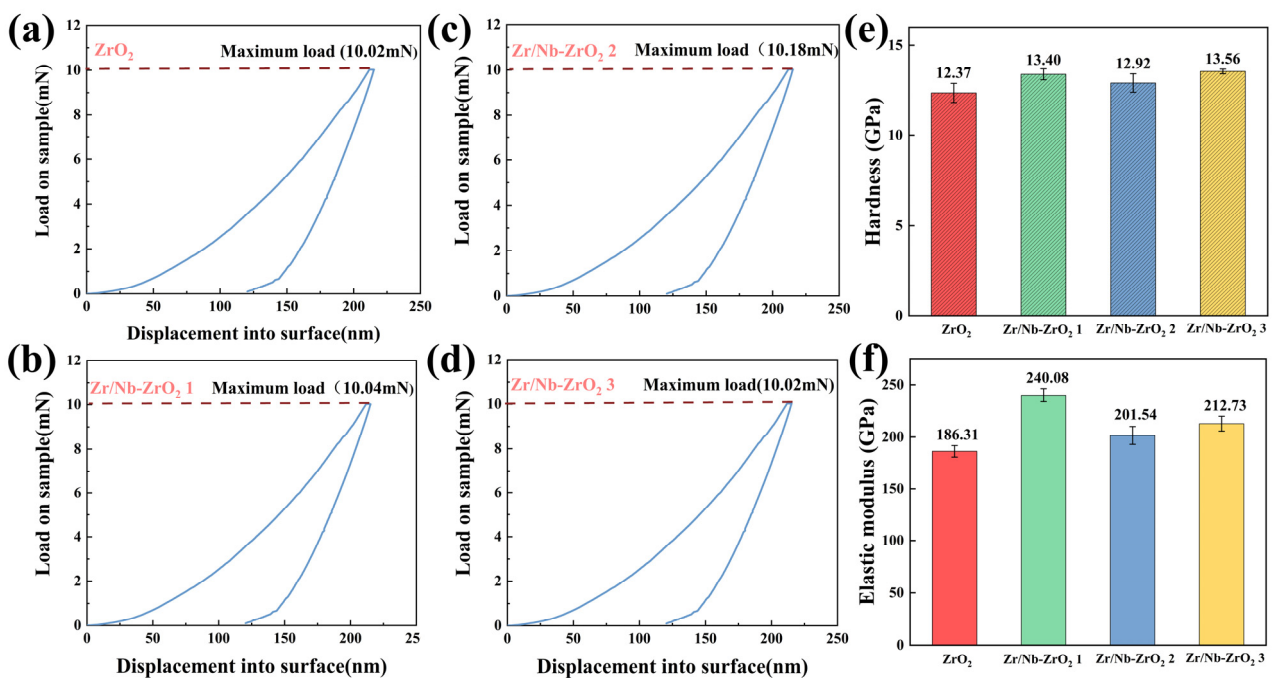


Figure 6. Loading–unloading cycle of (a) ZrO₂, (b) Zr/Nb-ZrO₂ 1, (c) Zr/Nb-ZrO₂ 2, and (d) Zr/Nb-ZrO₂ 3. (e) Hardnesses of four groups of samples. (f) Elastic moduli of four groups of samples.

3.2. Hydrophilicity and Corrosion Resistance

As shown in Figure 7, the contact angles measured by a contact angle goniometer for four sets of samples (Ti-6Al-4V, ZrO₂, Zr/Nb-ZrO₂ 1, Zr/Nb-ZrO₂ 2, Zr/Nb-ZrO₂ 3) were found to be 100.90°, 80.09°, 62.97°, 58.58°, and 64.68°, respectively. Notably, Zr/Nb-ZrO₂ 2 exhibited the smallest contact angle, indicating the highest hydrophilicity. Studies have shown a correlation between contact angle and surface roughness, where within a certain range, increased roughness corresponds to decreased contact angles [42]. This observation aligns with the AFM testing, which revealed that Zr/Nb-ZrO₂ 2 had the highest surface roughness.

For implant materials, greater corrosion resistance leads to longer lifespans. Figure 8 presents the polarization curves of the four sample sets. As indicated in Figure 8, when compared to titanium alloy, both ZrO₂ and Zr/Nb-ZrO₂ exhibited lower corrosion currents (I_{corr}) and higher corrosion potentials (E_{corr}). Remarkably, Zr/Nb-ZrO₂ 3 displayed the lowest corrosion current (I_{corr}) and the highest corrosion resistance. This can be attributed to two key factors. Firstly, following niobium ion implantation, the surface formed products primarily consisting of Nb₂O₅, known for its exceptional corrosion resistance [43]. Secondly,

the increase in surface roughness resulted in a larger contact area with the corrosive electrolyte, intensifying electrochemical corrosion interactions between metals [44].

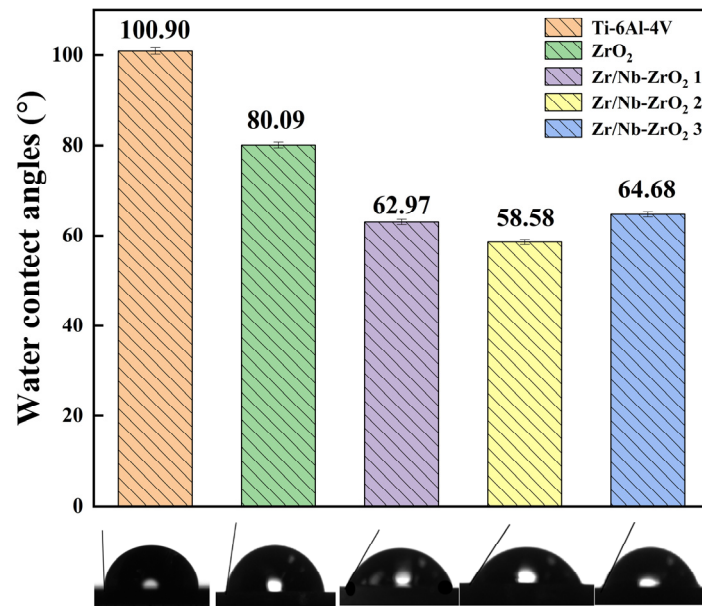


Figure 7. Water contact angle histogram of five groups.

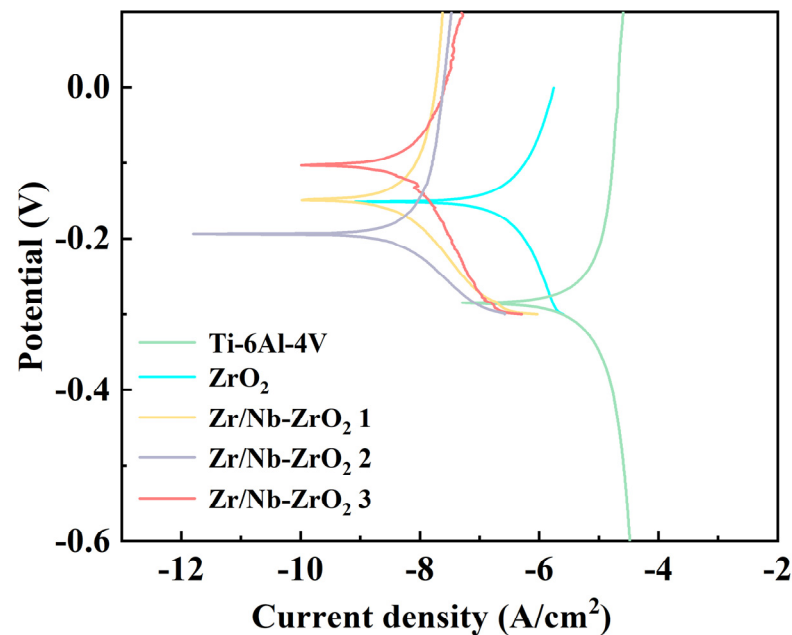


Figure 8. Polarization curves of five sample groups.

3.3. Structural Stability

3.3.1. Analysis of Formation and Binding Energies in the Zr/Nb-Doped ZrO₂ System

As shown in Figure 9a, Zr and Nb atoms were placed to replace Zr atoms in ZrO₂ at different ratios, illustrating the crystal cell diagrams of ZrO₂ and the cell diagrams after atomic substitution. The Zr concentration varied, reaching 0, 0.125, 0.50, 0.70, 0.80, and 0.90, while the Nb concentration ranged from 0, 0.01, 0.02, 0.03, 0.04, and 0.05, to 0.125. All of these crystal structures were optimized during the calculations. The formation energy of ZrO₂ material refers to the energy absorbed or released by the Zr and O atoms in their respective elemental states when they generate the ZrO₂ material. The difficulty of forming

a new Zr/Nb-ZrO₂ system by introducing Zr and Nb atoms into the ZrO₂ system can be assessed based on its formation energy. The formula is shown below:

$$E_{\text{form}} = E_{(\text{doped})} - E_{(\text{ZrO}_2)} - \sum E_{(\text{Zr/Nb doped})} + \sum E_{(\text{host})} \quad (1)$$

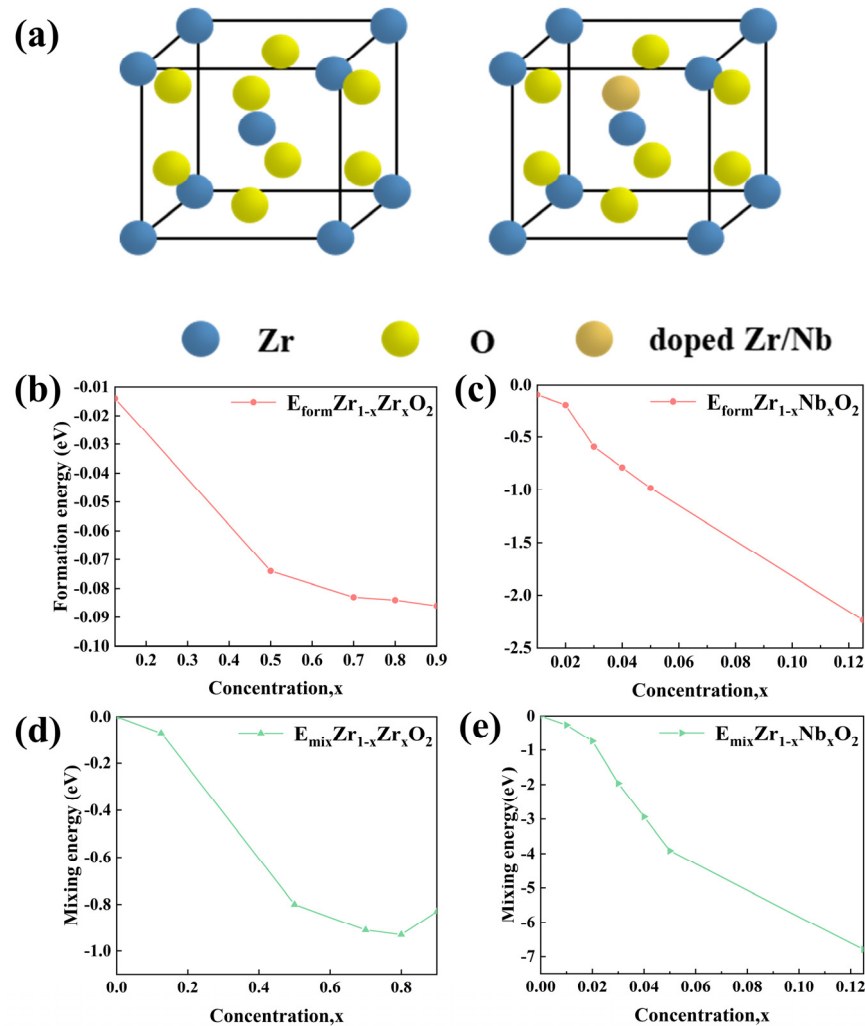


Figure 9. (a) Cell diagram of the Zr/Nb doping model. Formation energy (b) and binding energy (d) of different Zr concentrations; formation energy (c) and binding energy of different Nb concentrations (e).

In the above equation, E_{form} represents the formation energy of the new Zr/Nb-ZrO₂ system, $E_{(\text{doped})}$ is the total energy of the Zr/Nb-ZrO₂ new system after doping Zr/Nb atoms, $E_{(\text{ZrO}_2)}$ is the total energy of ZrO₂, $E_{(\text{Zr/Nb doped})}$ is the energy of the doped Zr/Nb atoms, and $E_{(\text{host})}$ is the energy of the Zr atom replaced in ZrO₂. It should be noted that the system and atomic energy mentioned above refer to the total energy of each respective system after structural optimization.

When the formation energy of the Zr/Nb-ZrO₂ new system is a negative value, it indicates that the new Zr/Nb-ZrO₂ system is relatively easy to form experimentally. Conversely, when the numerical value of the formation energy of the Zr/Nb-ZrO₂ new system is positive, it implies that the system is difficult to form because it requires the absorption of energy during the process [45]. As seen from Figure 9b,c, the formation energy values of all Zr/Nb-ZrO₂ new systems doped with Zr and Nb were negative, indicating that these Zr/Nb-ZrO₂ new systems are relatively easy to form.

To further investigate the structural stability of Zr and Nb atoms doped into the ZrO₂ system, this study also calculated the binding energy of the new Zr/Nb-ZrO₂ system. The

binding energy of the Zr/Nb-ZrO₂ system is the energy released when unbounded Zr and Nb atoms are doped into the ZrO₂ crystal structure. A more negative and larger absolute value of the binding energy for the Zr/Nb-ZrO₂ system implies greater structural stability. The formula for calculating the binding energy after doping is as follows:

$$E_{\text{mix}} = \frac{1}{\sum N_i} \left[E_{\text{total}} - \sum (N_i E_{\text{iso}}^i) \right] \quad (2)$$

In Figure 9d,e, it can be observed that with the increase in Zr/Nb content, the binding energy values of different Zr/Nb-ZrO₂ systems became increasingly negative, all falling below zero. Therefore, it is evident that the Zr/Nb-ZrO₂ systems exhibit excellent structural stability.

3.3.2. Mechanical Properties of Zr/Nb-Doped ZrO₂ System

Elastic constants are a crucial indicator of mechanical properties and a factor in demonstrating the stability of the crystal structure of Zr/Nb-doped ZrO₂ systems. The tetragonal ZrO₂ crystal structure studied in this paper has six independent elastic constants (C_{11} , C_{12} , C_{13} , C_{33} , C_{44} , and C_{66}). The objects of study achieve mechanical stability when the elastic constants satisfy the following conditions: $C_{11} > |C_{12}|$, $2C_{13}^2 < C_{33}(C_{11} + C_{12})$, $C_{44} > 0$, $C_{66} > 0$, and $2C_{16}^2 < C_{66}(C_{11} - C_{12})$.

In the CASTEP section, extensive first-principle calculations were conducted to obtain elastic constants for the Zr_{1-x}Zr_xO₂ and Zr_{1-x}Nb_xO₂ systems. The results, as shown in Tables 3 and 4, indicate that the systems doped with Zr and Nb atoms meet the conditions for mechanical stability. This aligns with the results of nanoindentation experiments and further confirms the mechanical stability of Zr/Nb-ZrO₂.

Table 3. The elastic constants of Zr_{1-x}Zr_xO₂.

Elastic Constant (C_{ij})	C_{11} /GPa	C_{33} /GPa	C_{44} /GPa	C_{66} /GPa	C_{12} /GPa	C_{13} /GPa	C_{16} /GPa
ZrO ₂	307.26	247.17	7.36	149.59	192.10	29.13	0.00
Zr _{0.875} Zr _{0.125} O ₂	319.71	288.53	4.00	148.59	190.03	31.01	0.00
Zr _{0.5} Zr _{0.5} O ₂	310.57	266.47	4.19	148.57	190.16	30.10	0.00
Zr _{0.3} Zr _{0.7} O ₂	306.76	278.66	5.33	148.53	190.10	25.61	0.00
Zr _{0.2} Zr _{0.8} O ₂	305.07	268.92	6.57	148.58	191.29	25.00	0.00
Zr _{0.1} Zr _{0.9} O ₂	305.99	281.38	6.77	148.61	191.12	25.86	0.00

Table 4. The elastic constants of Zr_{1-x}Nb_xO₂.

Elastic Constant (C_{ij})	C_{11} /GPa	C_{33} /GPa	C_{44} /GPa	C_{66} /GPa	C_{12} /GPa	C_{13} /GPa	C_{16} /GPa
ZrO ₂	307.26	247.17	7.36	149.59	192.10	29.13	0.00
Zr _{0.99} Nb _{0.01} O ₂	309.28	193.17	3.84	149.82	149.82	26.97	0.00
Zr _{0.98} Nb _{0.02} O ₂	313.15	223.66	1.52	148.88	194.41	30.81	0.00
Zr _{0.97} Nb _{0.03} O ₂	308.53	215.09	3.47	147.33	192.49	22.27	0.00
Zr _{0.96} Nb _{0.04} O ₂	308.44	200.82	4.82	146.07	199.26	29.51	0.00
Zr _{0.95} Nb _{0.05} O ₂	306.19	212.80	3.85	145.51	201.04	26.19	0.00
Zr _{0.875} Nb _{0.125} O ₂	274.79	203.89	8.89	138.22	215.85	32.97	0.00

The calculated elastic constants can be used to compute various other microscopic quantities, such as bulk modulus (B), shear modulus (G), Young's modulus (E), Poisson's ratio (ν), and the ratio of bulk to shear modulus [46]. These microscopic properties correspond to macroscopic performance indicators such as hardness, ease of processing, and mechanical strength. To further analyze the mechanical performance using the calculated elastic constants, the relationships of bulk modulus (B), shear modulus (G), Young's

modulus (E), and Poisson's ratio with the elastic constants can be determined using the Voigt–Reuss–Hill approximation method:

$$B = \frac{B_V + B_R}{2}, G = \frac{G_V + G_R}{2}, B_V = \frac{2}{9}(C_{11} + C_{22} + C_{33}), B_R = \frac{4}{9}(C_{12} + C_{13} + C_{23}), \quad (3)$$

$$G_V = \frac{2}{15}(C_{11} + C_{22} + C_{33} - C_{12} - C_{13} - C_{23}), G_R = \frac{2}{5}(C_{44} + C_{55} + C_{66}), \quad (4)$$

$$E = \frac{9GB}{3B + G}, \nu = \frac{3B - 2G}{2(3B + G)} \quad (5)$$

The bulk modulus (B) represents a material's ability to resist volume change under certain pressure conditions, indicating its resistance to deformation. A higher B value implies greater resistance to compression and, consequently, higher strength [47]. In Figure 10a, it can be observed that with the increasing Zr atom doping content, the B value of the $Zr_{1-x}Zr_xO_2$ system initially increased and then decreased, indicating that the system's resistance to compression and strength first increases and then decreases. The overall bulk modulus of the $Zr_{1-x}Zr_xO_2$ system was slightly higher than that of the ZrO_2 system, suggesting an increase in the system's resistance to compression and strength. Figure 10b shows that with the increasing Nb atom doping content, the bulk modulus of the $Zr_{1-x}Nb_xO_2$ system initially decreased and then increased. However, the overall bulk modulus of the $Zr_{1-x}Nb_xO_2$ system was slightly lower than that of the ZrO_2 system, indicating a decrease in the system's resistance to compression and strength. The shear modulus (G) is used to represent a material's resistance to shear strain, where a higher G value indicates greater shear strain resistance. Young's modulus (E) reflects a solid material's ability to resist deformation, with a higher E value indicating greater stiffness.

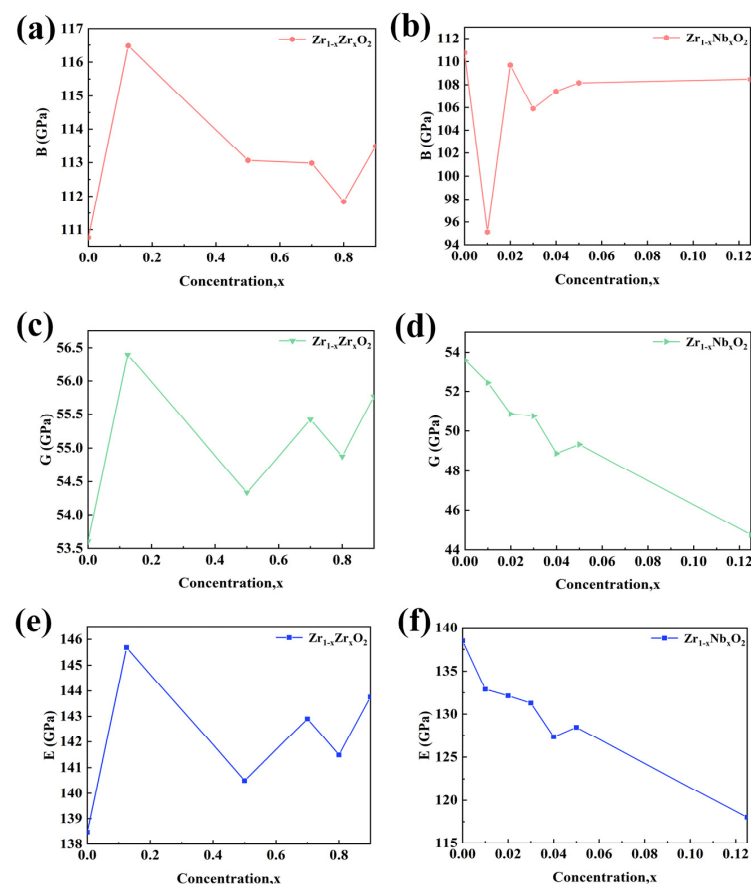


Figure 10. B (a), G (c), E (e) with different Zr concentrations; B (b), G (d), E (f) with different Nb concentrations.

In Figure 10c,e, it can be observed that with the increasing Zr atom doping content, the shear modulus and Young's modulus of the $Zr_{1-x}Zr_xO_2$ system initially increased and then decreased, signifying an initial increase followed by a decrease in the system's shear strain resistance and resistance to deformation. However, the overall values were slightly higher than those of the ZrO_2 system, indicating that the $Zr_{1-x}Zr_xO_2$ system has greater shear strain resistance and deformation resistance compared to the ZrO_2 system. Conversely, in Figure 10d,f, with increasing Nb atom doping content, the shear modulus and Young's modulus of the $Zr_{1-x}Nb_xO_2$ system decreased, indicating a decrease in the system's resistance to compression and deformation, resulting in reduced stiffness. This is consistent with the analysis of nanoindentation-related experimental results.

3.3.3. The Electronic Density of States (DOS) and Partial Density of States (PDOS) for the Zr/Nb-Doped ZrO_2 System

In order to gain further insights into the influence of Zr and Nb atomic doping concentrations on the structural stability of the ZrO_2 system, the DOS and PDOS were calculated and plotted for the new Zr/Nb- ZrO_2 system to analyze its electronic properties.

Figure 11a,b depict the total density-of-states curves for different systems with Zr and Nb atomic doping, respectively. It can be observed that the shapes of the total density-of-states plots for $Zr_{1-x}Zr_xO_2$ and $Zr_{1-x}Nb_xO_2$ systems, after Zr and Nb doping, are similar, indicating that the energy level structure of the systems remained unchanged upon Zr and Nb doping. The presence of non-zero electron density at the Fermi level implies that these systems exhibit certain metallic characteristics. Upon introducing Zr and Nb atoms into the $Zr_{1-x}Zr_xO_2$ and $Zr_{1-x}Nb_xO_2$ systems, the electron density at the Fermi level increased, indicating a reduction in the electrochemical stability of these systems compared to ZrO_2 .

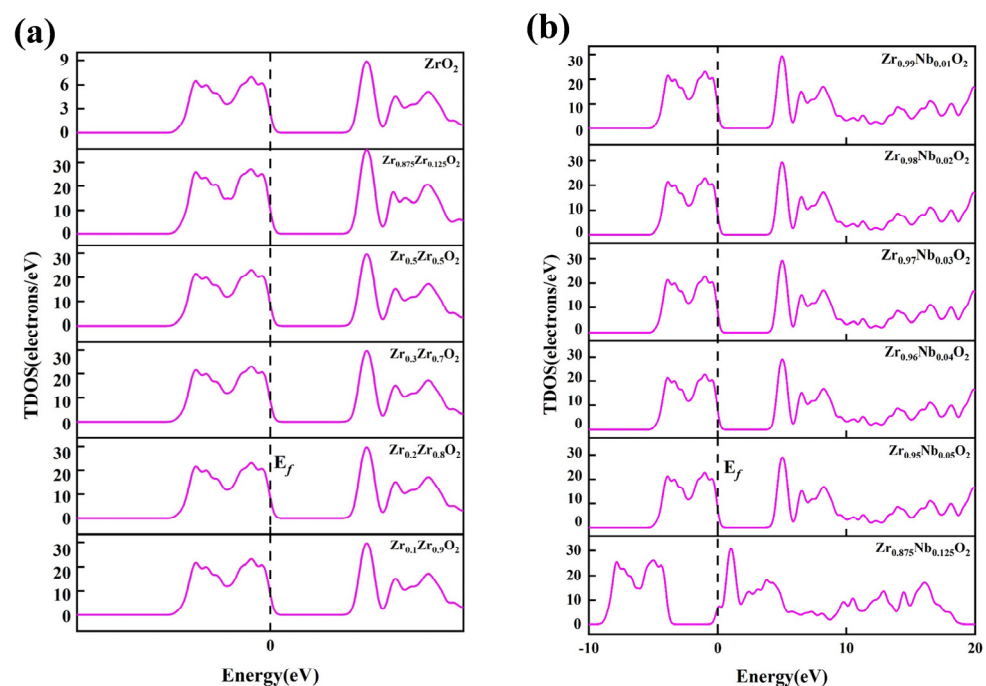


Figure 11. Total density of states of the new Zr/Nb- ZrO_2 system: (a) $Zr_{1-x}Zr_xO_2$, (b) $Zr_{1-x}Nb_xO_2$.

In the case of the $Zr_{1-x}Zr_xO_2$ system, with an increase in Zr atomic doping concentration, the electron density at the Fermi level initially decreased and then increased, suggesting an improvement of and subsequent reduction in electrochemical stability. Conversely, in the $Zr_{1-x}Nb_xO_2$ system, as the Nb atomic doping concentration increased, the electron density at the Fermi level decreased, indicating an enhancement in electrochemical stability. Notably, for the $Zr_{0.875}Nb_{0.125}O_2$ system, corresponding to a Nb atomic concentration of 0.125, the total DOS exhibited a peak shift towards lower energy levels, indicating

increased structural stability [48]. Furthermore, the DOS near the Fermi level for both systems exhibited an increase relative to the DOS of ZrO_2 .

Figure 12a,b illustrates the PDOS for Zr and O in the $Zr_{1-x}Zr_xO_2$ system. Both the ZrO_2 and $Zr_{1-x}Zr_xO_2$ DOS profiles exhibit three regions: the lowest-energy peak, relatively flat and with low peak height, primarily arising from localized s electrons of O atoms and p orbitals of Zr atoms; the bonding region near the Fermi level, encompassing contributions from Zr3d and O2p orbitals, indicating covalent bonding; and the hybridization peaks at the top of the DOS.

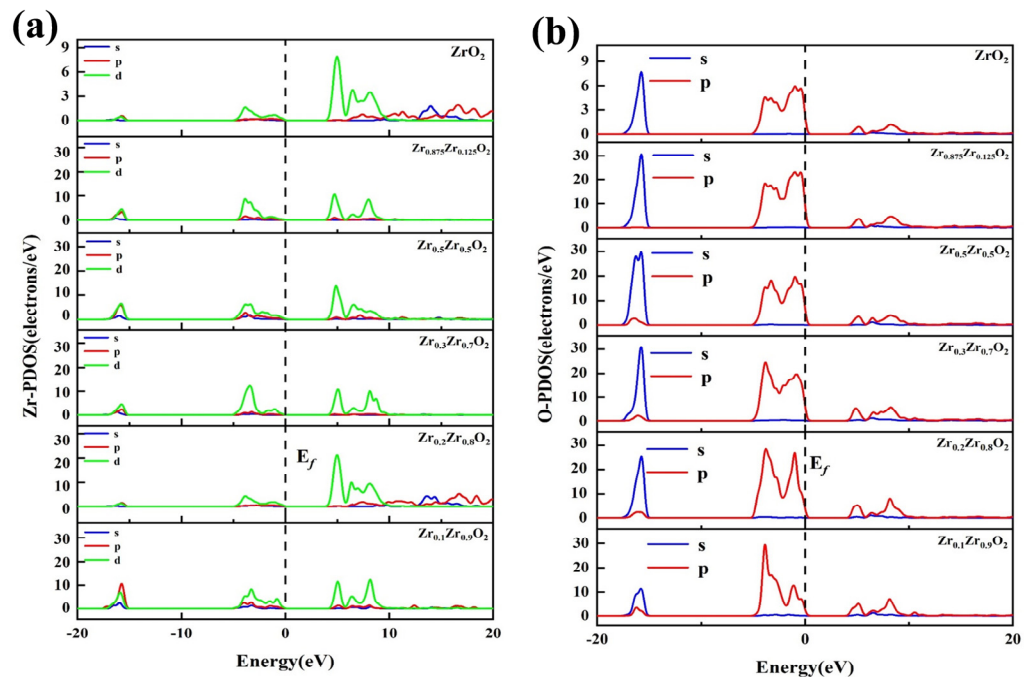


Figure 12. Partial density of states (PDOS) of the $Zr_{1-x}Zr_xO_2$ system: (a) Zr-PDOS, (b) O-PDOS.

The hybridization of Zr3d and O2p orbitals suggests the presence of covalent bonding. Typically, peak values near the ground state energy level have a minimal impact on the macroscopic material properties. On the other hand, the electron distribution in the vicinity of the Fermi level is of significant research interest, as it can exert a substantial influence on macroscopic properties. Therefore, the focus is mainly on the electron distribution near the Fermi level. In Figure 12a,b, it is shown that with an increase in Zr concentration, the hybridization of Zr3d and O2p orbitals in the $Zr_{1-x}Zr_xO_2$ system was initially strengthened, and then weakened. Consequently, its structural stability first increased and then decreased as well.

Figure 13a–c shows the PDOS for Zr, Nb, and O in the $Zr_{1-x}Nb_xO_2$ system. In the electron region near the Fermi level, the hybridization of p-p orbitals was strengthened as the peak height decreased, while the hybridization of p-d orbitals was strengthened as the peak height increased. With an increase in Nb concentration, the $Zr_{1-x}Nb_xO_2$ system exhibited increased peak values for Zr3d, Nb3d, and O2p orbitals, indicating enhanced orbital hybridization. Consequently, its structural stability increased. As the Nb doping concentration increased, both the TDOS and the PDOS shifted towards lower energy levels. At higher doping concentrations, the impurity atoms were close to each other, resulting in a pronounced hybridization of electrons in Zr3d, Nb3d, and O2p orbitals. This enhanced hybridization strengthened the interaction between these orbitals [49,50]. As the concentration increased, the system tended more towards the properties of $Zr_{1-x}Nb_xO_2$, making it easier for the system to reach a stable state. This was also a contributing factor to the greater stability of this system compared to $Zr_{1-x}Zr_xO_2$. These findings align with the analysis of binding energy and TDOS. Therefore, the enhanced orbital hybridization and

increased interaction between bonds lead to the formation of a more stable new system. Consequently, the process exhibited improved macroscopic properties, as is consistent with previous experimental results.

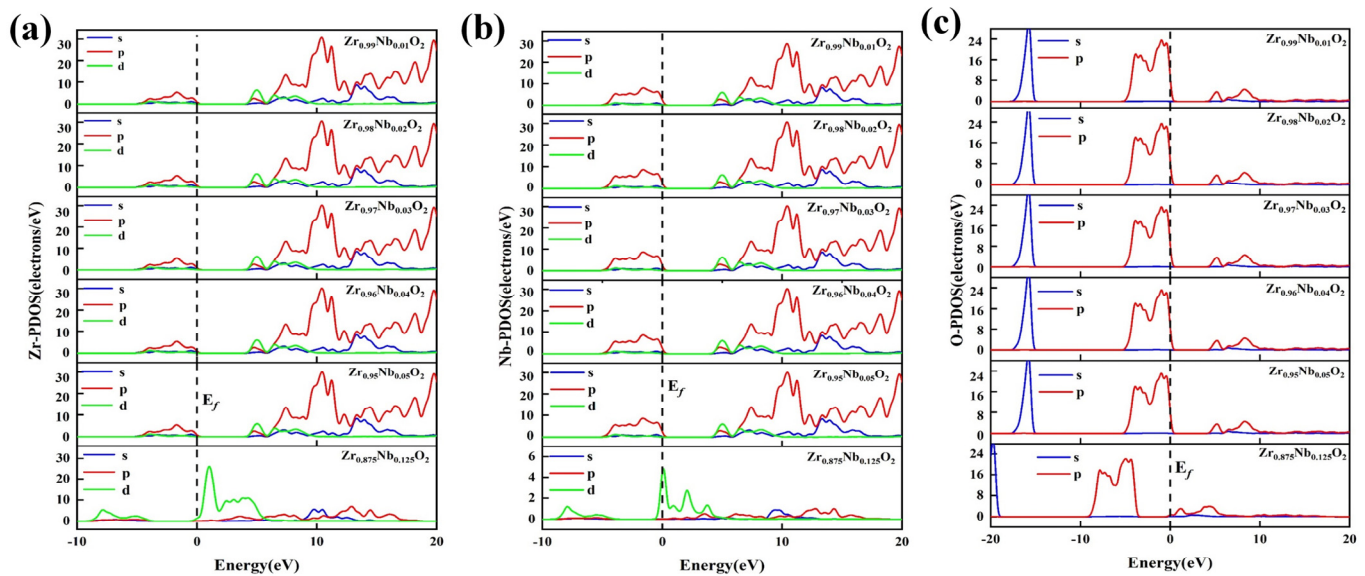


Figure 13. Partial density of states (PDOS) of the $Zr_{1-x}Nb_xO_2$ system: (a) Zr-PDOS, (b) Nb-PDOS, (c) O-PDOS.

4. Conclusions

In this study, Zr and Nb ions were co-implanted into ZrO_2 thin films using an RF magnetron sputtering system and a plasma immersion ion implantation system. Under the same implantation energy, different ion doses were utilized to obtain three sets of Zr/Nb- ZrO_2 samples: Zr/Nb- ZrO_2 1 (50 min), Zr/Nb- ZrO_2 2 (60 min), and Zr/Nb- ZrO_2 3 (70 min). The hardnesses and elastic moduli of the three sets of Zr/Nb- ZrO_2 samples were moderately improved, with the maximum hardness values reaching 13.569 GPa and the highest elastic modulus recorded at 240.08 GPa. Zr/Nb- ZrO_2 samples exhibited superior hydrophilicity and corrosion resistance compared to pure ZrO_2 , with Zr/Nb- ZrO_2 3 demonstrating the strongest corrosion resistance and Zr/Nb- ZrO_2 2 displaying the best hydrophilicity. Our calculations demonstrated that with increasing Zr and Nb doping concentrations, Nb-doped systems exhibited lower formation energies and better ductility and stability, making them easier to form and more stable. As the doping concentration changed, the hybridization also varied, leading to an increase in the total density of states. Consequently, the orbital hybridization between orbitals strengthened, as did the interactions between bonds, resulting in a more stable new system. With increasing concentration, the newly formed systems exhibited properties closer to $Zr_{1-x}Nb_xO_2$, making it easier to achieve a stable state compared to the $Zr_{1-x}Zr_xO_2$ system. This study successfully combined theoretical explanations with experimental evidence, providing a more comprehensive understanding of ZrO_2 -modified materials. This marks an important step forward in the application of Zr/Nb- ZrO_2 in bio-implant coating materials.

Author Contributions: Design and direction, D.L.; software, L.W. and Y.G.; data curation, L.W.; writing—original draft preparation, Y.G.; writing—review and editing, D.L.; supervision, D.L. All authors have read and agreed to the published version of the manuscript.

Funding: This research was funded by National Natural Science Foundation of China, grant number 51772209, Tianjin Research Innovation Project for Postgraduate Students, grant number 2022SKYZ152 and Tianjin Normal University Research Innovation Project for Postgraduate Students, grant number 2022KYCX100Y).

Institutional Review Board Statement: Not applicable.

Informed Consent Statement: Not applicable.

Data Availability Statement: Not applicable.

Conflicts of Interest: The authors declare no conflict of interest.

References

1. Gomes, A.L.; Montero, J. Zirconia Implant Abutments: A Review. *Med. Oral* **2011**, *16*, e50–e55. [[CrossRef](#)] [[PubMed](#)]
2. Ehrhart, G.; Capoen, B.; Robbe, O.; Boy, P.; Turrell, S.; Bouazaoui, M. Structural and Optical Properties of N-Propoxide Sol–Gel Derived ZrO₂ Thin Films. *Thin Solid Films* **2006**, *496*, 227–233. [[CrossRef](#)]
3. Hembram, K.P.S.S.; Dutta, G.; Waghmare, U.V.; Mohan Rao, G. Electrical and Structural Properties of Zirconia Thin Films Prepared by Reactive Magnetron Sputtering. *Phys. B Condens. Matter* **2007**, *399*, 21–26. [[CrossRef](#)]
4. Nemati, A.; Saghafi, M.; Khamseh, S.; Alibakhshi, E.; Zarrintaj, P.; Saeb, M.R. Magnetron-Sputtered Ti₂Ny Thin Films Applied on Titanium-Based Alloys for Biomedical Applications: Composition-Microstructure-Property Relationships. *Surf. Coat. Technol.* **2018**, *349*, 251–259. [[CrossRef](#)]
5. Zalnezhad, E. Effect of Structural Evolution on Mechanical Properties of ZrO₂ Coated Ti–6Al–7Nb-Biomedical Application. *Appl. Surf. Sci.* **2016**, *370*, 32–39. [[CrossRef](#)]
6. Pamu, D.; Sudheendran, K.; Krishna, M.G.; Raju, K.C.J.; Bhatnagar, A.K. Ambient Temperature Stabilization of Crystalline Zirconia Thin Films Deposited by Direct Current Magnetron Sputtering. *Thin Solid Films* **2009**, *517*, 1587–1591. [[CrossRef](#)]
7. Saleem, S.; Ahmad, R.; Ayub, R.; Ikhlaiq, U.; Jin, W.; Chu, P.K. Investigation of Nano-Structured Zirconium Oxide Film on Ti6Al4V Substrate to Improve Tribological Properties Prepared by PIII&D. *Appl. Surf. Sci.* **2017**, *394*, 586–597. [[CrossRef](#)]
8. Chauhan, V.; Gupta, D.; Upadhyay, S.; Mahajan, A.; Gaur, A.; Kumar, S.; Kumar, R. Influence of High Dose Gamma Radiation on Optical, Physico-Chemical and Surface Morphology Properties of Nanocrystalline ZrO₂ Thin Films. *Opt. Mater.* **2022**, *126*, 112125. [[CrossRef](#)]
9. Alin, M. Comprehensive Study of Changes in the Optical, Structural and Strength Properties of ZrO₂ Ceramics as a Result of Phase Transformations Caused by Irradiation with Heavy Ions. *J. Mater. Sci.* **2021**, *32*, 17810–17821. [[CrossRef](#)]
10. Ananchenko, D.V.; Nikiforov, S.V.; Sobyenin, K.V.; Konev, S.F.; Dauletbekova, A.K.; Akhmetova-Abdik, G.; Akilbekov, A.T.; Popov, A.I. Paramagnetic Defects and Thermoluminescence in Irradiated Nanostructured Monoclinic Zirconium Dioxide. *Materials* **2022**, *15*, 8624. [[CrossRef](#)]
11. Fu, X.M. The Influence of the Hydrothermal Temperature on the Morphologies and the Optical Absorption Properties of M-ZrO₂ Nanoparticles. *Appl. Mech. Mater.* **2013**, *320*, 11–14. [[CrossRef](#)]
12. Saudé, S.; Grynszpan, R.I.; Anwand, W.; Brauer, G. Defect Production in Ion-Implanted Yttria-Stabilized Zirconia Investigated by Positron Depth Profiling. *J. Alloys Compd.* **2004**, *382*, 252–256. [[CrossRef](#)]
13. Zhang, H.H.; Ma, C.Y.; Zhang, Q.Y. Scaling Behavior and Structure Transition of ZrO₂ Films Deposited by RF Magnetron Sputtering. *Vacuum* **2009**, *83*, 1311–1316. [[CrossRef](#)]
14. Yang, J.; Wang, M.; Li, X.; Dong, Z.; Zhou, X.; Luan, J.; Guo, Y.; Xue, Y. Structural and Electrochemical Corrosion Studies of Spin Coated ZrO₂ Thin Films over Stainless Steel Alloy for Bone Defect Applications. *J. Appl. Biomater. Funct. Mater.* **2022**, *20*, 228080002110667. [[CrossRef](#)] [[PubMed](#)]
15. Abd El-Aal, M.; Seto, T. Surface-Enhanced Raman Scattering and Catalytic Activity Studies over Nanostructured Au–Pd Alloy Films Prepared by DC Magnetron Sputtering. *Res. Chem. Intermed.* **2020**, *46*, 3741–3756. [[CrossRef](#)]
16. Tallarico, D.A.; Gobbi, A.L.; Paulin Filho, P.I.; Maia Da Costa, M.E.H.; Nascete, P.A.P. Growth and Surface Characterization of TiNbZr Thin Films Deposited by Magnetron Sputtering for Biomedical Applications. *Mater. Sci. Eng. C* **2014**, *43*, 45–49. [[CrossRef](#)]
17. Photiou, D.; Panagiotopoulos, N.T.; Koutsokeras, L.; Evangelakis, G.A.; Constantinides, G. Microstructure and Nanomechanical Properties of Magnetron Sputtered Ti–Nb Films. *Surf. Coat. Technol.* **2016**, *302*, 310–319. [[CrossRef](#)]
18. Luo, P.; Wang, S.-N.; Zhao, T.-T.; Li, Y. Surface Characteristics, Corrosion Behavior, and Antibacterial Property of Ag-Implanted NiTi Alloy. *Rare Met.* **2013**, *32*, 113–121. [[CrossRef](#)]
19. Kazemi, M.; Ahangarani, S.; Esmailian, M.; Shanaghi, A. Investigation on the Corrosion Behavior and Biocompatibility of Ti-6Al-4V Implant Coated with HA/TiN Dual Layer for Medical Applications. *Surf. Coat. Technol.* **2020**, *397*, 126044. [[CrossRef](#)]
20. Li, Q.; Zhao, M.; Li, L.; Dong, L.; Wu, J.; Li, D. Co-Regulation of Cu/Zn Contents Enhanced the Biological and Mechanical Properties of TiN Coated Ti-6Al-4V Alloy. *Surf. Coat. Technol.* **2020**, *395*, 125943. [[CrossRef](#)]
21. Padervand, M.; Ghasemi, S.; Hajiahmadi, S.; Wang, C. K₄Nb₆O₁₇/Fe₃N/α-Fe₂O₃/C₃N₄ as an Enhanced Visible Light-Driven Quaternary Photocatalyst for Acetamiprid Photodegradation, CO₂ Reduction, and Cancer Cells Treatment. *Appl. Surf. Sci.* **2021**, *544*, 148939. [[CrossRef](#)]
22. Gao, T.; Lin, J.; Zhang, K.; Padervand, M.; Zhang, Y.; Zhang, W.; Shi, M.; Wang, C. Porous Defective Bi/Bi₃NbO₇ Nanosheets for Efficient Photocatalytic NO Removal under Visible Light. *Processes* **2022**, *11*, 115. [[CrossRef](#)]
23. Xue, C.; Zhang, P.; Wei, D.; Hu, H.; Li, F.; Yang, K. Corrosion and Tribocorrosion Behaviors for TA3 in Ringer’s Solution after Implantation of Nb Ions. *Appl. Sci.* **2020**, *10*, 8329. [[CrossRef](#)]

24. Zhao, T.; Li, Y.; Xiang, Y.; Zhao, X.; Zhang, T. Surface Characteristics, Nano-Indentation and Corrosion Behavior of Nb Implanted NiTi Alloy. *Surf. Coat. Technol.* **2011**, *205*, 4404–4410. [[CrossRef](#)]
25. Liu, Y.Z.; Zu, X.T.; Li, C.; Qiu, S.Y.; Huang, X.Q.; Wang, L.M. Surface Characteristics and Corrosion Behavior of Ti–Al–Zr Alloy Implanted with Al and Nb. *Corros. Sci.* **2007**, *49*, 1069–1080. [[CrossRef](#)]
26. Liang, T.; Zeng, L.; Shi, Y.; Pan, H.; Chu, P.K.; Yeung, K.W.K.; Zhao, Y. In Vitro and in Vivo Antibacterial Performance of Zr & O PIII Magnesium Alloys with High Concentration of Oxygen Vacancies. *Bioact. Mater.* **2021**, *6*, 3049–3061. [[CrossRef](#)]
27. Muhammad, I.D.; Awang, M.; Mamat, O.; Shaari, Z.B. First-Principles Calculations of the Structural, Mechanical and Thermodynamics Properties of Cubic Zirconia. *World J. Nano Sci. Eng.* **2014**, *04*, 97–103. [[CrossRef](#)]
28. Perdew, J.P.; Burke, K.; Ernzerhof, M. Generalized Gradient Approximation Made Simple. *Phys. Rev. Lett.* **1996**, *77*, 3865–3868. [[CrossRef](#)]
29. Pettifor, D.G. Theoretical Predictions of Structure and Related Properties of Intermetallics. *Mater. Sci. Technol.* **1992**, *8*, 345–349. [[CrossRef](#)]
30. Song, X.; Zhao, M.; Li, D. Controllable Ag/Ta Ratios of Co-Implanted TiN Films on Titanium Alloys for Osteogenic Enhancement and Antibacterial Responses. *Surf. Coat. Technol.* **2022**, *436*, 128294. [[CrossRef](#)]
31. Meganathan, P.; Selvaraj, L.M.; Peter, L.S.; Venkatachalam, S.; Srinivasan, N. Synergetic Surface Behavior of Sol–Gel ZrO₂–Nb₂O₅ Coated 316L Stainless Steel for Biomedical Applications. *J. Bio-Tribo-Corros.* **2020**, *6*, 108. [[CrossRef](#)]
32. Fathy, A.; Elkady, O.; Abu-Oqail, A. Microstructure, Mechanical and Wear Properties of Cu–ZrO₂ Nanocomposites. *Mater. Sci. Technol.* **2017**, *33*, 2138–2146. [[CrossRef](#)]
33. Medicherla, V.R.R.; Majumder, S.; Paramanik, D.; Varma, S. Formation of Self-Organized Ta Nano-Structures by Argon Ion Sputtering of Ta Foil: XPS and AFM Study. *J. Electron Spectrosc. Relat. Phenom.* **2010**, *180*, 1–5. [[CrossRef](#)]
34. Li, F.; Wei, D.; Zhang, P.; Chen, X.; Ding, F.; Wang, S.; Zhao, R.; Wang, Z. Effects of Zr Ion Implantation on Crystal Structure and Nanoindentation Behavior of TC18 Titanium Alloy. *Mater. Res. Express* **2018**, *6*, 026560. [[CrossRef](#)]
35. Reddy, B.M.; Chowdhury, B.; Smirniotis, P.G. An XPS Study of the Dispersion of MoO₃ on TiO₂–ZrO₂, TiO₂–SiO₂, TiO₂–Al₂O₃, SiO₂–ZrO₂, and SiO₂–TiO₂–ZrO₂ Mixed Oxides. *Appl. Catal. Gen.* **2001**, *211*, 19–30. [[CrossRef](#)]
36. Cordeiro, J.M.; Beline, T.; Ribeiro, A.L.R.; Rangel, E.C.; Da Cruz, N.C.; Landers, R.; Faverani, L.P.; Vaz, L.G.; Fais, L.M.G.; Vicente, F.B.; et al. Development of Binary and Ternary Titanium Alloys for Dental Implants. *Dent. Mater.* **2017**, *33*, 1244–1257. [[CrossRef](#)]
37. Hoppe, V.; Szymczyk-Ziółkowska, P.; Rusińska, M.; Dybała, B.; Poradowski, D.; Janeczek, M. Assessment of Mechanical, Chemical, and Biological Properties of Ti–Nb–Zr Alloy for Medical Applications. *Materials* **2020**, *14*, 126. [[CrossRef](#)]
38. Ge, Y.; Wang, Y.; Chen, J.; Zou, Y.; Guo, L.; Ouyang, J.; Jia, D.; Zhou, Y. Hot Corrosion Behavior of NbSi₂/SiO₂–Nb₂O₅ Multilayer Coating on Nb Alloy. *J. Alloys Compd.* **2018**, *767*, 7–15. [[CrossRef](#)]
39. Olsson, C.-O.A.; Landolt, D. Atmospheric Oxidation of a Nb–Zr Alloy Studied with XPS. *Corros. Sci.* **2004**, *46*, 213–224. [[CrossRef](#)]
40. Alfonso, J.E.; Buitrago, J.; Torres, J.; Marco, J.F.; Santos, B. Influence of Fabrication Parameters on Crystallization, Microstructure, and Surface Composition of NbN Thin Films Deposited by Rf Magnetron Sputtering. *J. Mater. Sci.* **2010**, *45*, 5528–5533. [[CrossRef](#)]
41. Smyrnova, K.; Sahul, M.; Haršani, M.; Pogrebniak, A.; Ivashchenko, V.; Beresnev, V.; Stolbovoy, V.; Čaplovič, L.; Čaplovičová, M.; Vančo, L.; et al. Microstructure, Mechanical and Tribological Properties of Advanced Layered WN/MeN (Me = Zr, Cr, Mo, Nb) Nanocomposite Coatings. *Nanomaterials* **2022**, *12*, 395. [[CrossRef](#)] [[PubMed](#)]
42. Zhao, M.; Ji, X.; Li, D. Ag⁺ and Ca⁺ Single Implantation and Co-Implantation Induced the Cell Growth and Antibacterial Activity of TiN/Ti-6Al-4V. *Vacuum* **2023**, *207*, 111579. [[CrossRef](#)]
43. Zhou, F.Y.; Wang, B.L.; Qiu, K.J.; Lin, W.J.; Li, L.; Wang, Y.B.; Nie, F.L.; Zheng, Y.F. Microstructure, Corrosion Behavior and Cytotoxicity of Zr–Nb Alloys for Biomedical Application. *Mater. Sci. Eng. C* **2012**, *32*, 851–857. [[CrossRef](#)]
44. Li, K.; Li, Y.; Huang, X.; Gibson, D.; Zheng, Y.; Liu, J.; Sun, L.; Fu, Y.Q. Surface Microstructures and Corrosion Resistance of Ni–Ti–Nb Shape Memory Thin Films. *Appl. Surf. Sci.* **2017**, *414*, 63–67. [[CrossRef](#)]
45. Yuan, Z.-P.; Cui, H.-B.; Guo, X.-F. First-Principles Calculation of Point-Defective Structures of B2–NiSc Intermetallics. *Radiat. Eff. Defects Solids* **2016**, *171*, 668–677. [[CrossRef](#)]
46. Benyelloul, K.; Aourag, H. Elastic Constants of Austenitic Stainless Steel: Investigation by the First-Principles Calculations and the Artificial Neural Network Approach. *Comput. Mater. Sci.* **2013**, *67*, 353–358. [[CrossRef](#)]
47. Tan, X.; Li, X.; Wang, Y.; Liu, X.; Yu, C.; Ren, Y. Ab-Initio Study on the Stability, Electronic and Mechanical Properties of Transition Metal Nitrides under External Pressure. *Solid State Sci.* **2017**, *66*, 16–22. [[CrossRef](#)]
48. Jhi, S.-H.; Ihm, J.; Louie, S.G.; Cohen, M.L. Electronic Mechanism of Hardness Enhancement in Transition-Metal Carbonitrides. *Nature* **1999**, *399*, 132–134. [[CrossRef](#)]
49. French, R.H.; Glass, S.J.; Ohuchi, F.S.; Xu, Y.-N.; Ching, W.Y. Experimental and Theoretical Determination of the Electronic Structure and Optical Properties of Three Phases of ZrO₂. *Phys. Rev. B* **1994**, *49*, 5133–5142. [[CrossRef](#)]
50. Robertson, J.; Xiong, K.; Clark, S.J. Band Structure of Functional Oxides by Screened Exchange and the Weighted Density Approximation. *Phys. Status Solidi B* **2006**, *243*, 2054–2070. [[CrossRef](#)]

Disclaimer/Publisher’s Note: The statements, opinions and data contained in all publications are solely those of the individual author(s) and contributor(s) and not of MDPI and/or the editor(s). MDPI and/or the editor(s) disclaim responsibility for any injury to people or property resulting from any ideas, methods, instructions or products referred to in the content.